LITHOS 456–457 (2023) 107325

Contents lists available at ScienceDirect

LITHOS

journal homepage: www.elsevier.com/locate/lithos

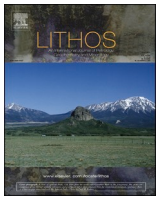

Large silicic magma chambers at the Moho depth characterize the multi-level plumbing system of back-arc spreading ridges

Emanuela Gennaro [a,*], Gianluca Iezzi [a,b], Luca Cocchi [b], Guido Ventura [b]

[a] Dipartimento di Ingegneria & Geologia (InGeO), Università G. D'Annunzio di Chieti-Pescara, Via dei Vestini 31, 66100 Chieti, Italy
[b] Istituto Nazionale di Geofisica e Vulcanologia, Via di Vigna Murata 605, 00143 Roma, Italy

ARTICLE INFO

Keywords:
Spreading ridges
Petrology
Geophysics
Modelling
Plumbing system

ABSTRACT

The plumbing system of volcanoes in crustal convergent settings consists of vertically superimposed, sill-like reservoirs. The shallower reservoirs are generally filled by less dense and SiO_2-richer magmas. The plumbing systems of spreading ridges are supposed to be simpler and characterized by prevailing sub-parallel vertical dykes. Here, we present the results of thermo-barometric determinations from minerals and modelling of potential field data at the Marsili spreading ridge in the Southern Tyrrhenian Sea back-arc oceanic basin. The Marsili plumbing system consists of sill-like, large SiO_2-rich magma reservoirs located at the Moho depth and sub-vertical basaltic dykes crossing the whole oceanic crust. The formation of deep-seated silicic reservoirs is associated with a decrease in the back-arc spreading rate. The geometry of the plumbing system of spreading ridges may be not dissimilar from that of volcanoes at convergent margins.

1. Introduction

The magma plumbing system of continental arc volcanoes commonly consists of a deep storage zone stowed in the lithospheric mantle, and of shallower, crustal and vertically interconnected reservoirs with different crystal/melt amounts (Annen et al., 2015; Cruden and Weinberg, 2018; Hildreth, 2004; Magee et al., 2018; Sparks et al., 2012). The deeper storage zone is characterized by H_2O-poor basaltic magmas while the shallower crustal reservoirs host more evolved and hydrated magmas (Cashman et al., 2017). The plumbing systems of oceanic spreading ridges are supposed to be simpler than those of continental volcanoes because of the reduced thickness of the oceanic crust, although they may be also characterized by vertically superimposed magma reservoirs (Bennett et al., 2019; Lissenberg and MacLeod, 2016; Wanless and Shaw, 2012). These reservoirs usually host poorly evolved, mainly basaltic magmas, but plagiogranites associated with the melting of gabbros have been occasionally found at the interface between the oceanic dyke complex and the lower oceanic crust (Koepke et al., 2007; Rollinson, 2014). In addition, rhyolites originated from the fractionation of MORB (Mid-Ocean Ridge Basalts)-like basalts have been recognized on the Alarcon Rise (Portner et al., 2022). However, the storage depth of magmas with different composition and the inner structure of spreading ridges are still poorly constrained and mostly unknown because of the lack of coupled geophysical and geochemical data (Magee et al., 2018). In particular, an open question concerns the location of possible magma chambers hosting evolved magmas with important implications for the mechanisms of the accretion and evolution of the oceanic crust. Here, we report combined petrological and potential field (gravity and magnetic) data on the Marsili axial volcano (MAV, Southern Tyrrhenian Sea, Italy), which represents the ridge of the homonymous oceanic back-arc basin associated with the subduction of the Ionian Sea below the Calabrian Arc (Fig. 1a, b; Corradino et al., 2022; Marani and Trua, 2002; Rosenbaum and Lister, 2004; Ventura et al., 2013). MAV is a NNW-SSE elongated, 70 × 30 km ridge rising 3200 m from the seafloor. The top of the ridge is at about 500 m b.s.l. (Fig. 1a, b). MAV formed in the last 1 Ma on the ~10–12 km thick oceanic crust of the 2 Ma old oceanic Marsili back-arc basin (Cocchi et al., 2009) and last erupted about 2–3 ka BP (Iezzi et al., 2014, 2020; Tamburrino et al., 2015). MAV is characterized by NNW-SSE striking dykes and aligned cones, and the erupted products consist of lava flows and more recent tephra. The MAV accretion rate during the Brunhes chron (0–0.78 Ma) is about 4×10^{-3} km^{-3} yr^{-1} (Cocchi et al., 2009). At the present, MAV is characterized by shallow seismicity and hydrothermal activity (D'Alessandro et al., 2009, 2012; Lupton et al., 2011). The MAV rocks range in composition from basalts with IAB (Island Arc Basalts) and OIB (Ocean Island Basalts) affinity to trachytes with a sub-alkaline affinity (Trua et al., 2002, 2011). The

* Corresponding author.
E-mail address: emanuela.gennaro@unich.it (E. Gennaro).

https://doi.org/10.1016/j.lithos.2023.107325
Received 7 March 2023; Received in revised form 10 August 2023; Accepted 13 August 2023
Available online 16 August 2023

crystal-chemistry of plagioclases and clinopyroxenes suggests the prevalence of fractional crystallization processes and minor mixing between OIB- and IAB-type basalts (Trua and Marani, 2021). Data on olivine crystals of some MAV basalts and basaltic andesites show that these magmas rose to the surface on time scales ranging from years to days depending on the storage time within the volcano and the degree of interaction with crystal-mush zones (Albert et al., 2022).

Our results from petrological and geophysical data unveil that the MAV plumbing system consists of reservoirs stored at different levels in the oceanic crust and within the volcanic edifice. Unexpectedly, the most evolved magma is stored in reservoirs located at the Moho depth, while the progressively less evolved magmas accumulate preferentially at shallower depths. Also, the mafic magmas fed lava flows and dykes whereas the felsic magmas also fed low energy explosive eruptions (Iezzi et al., 2020; Tamburrino et al., 2015). This has important implications for the knowledge of the multi-level plumbing system of spreading ridges and the mechanisms of formation and growth of the oceanic crust in back-arc basins. The proposed integrated petrological and geophysical datasets provide an opportunity to decipher the structure and evolution of the magma plumbing systems at spreading centres.

2. Materials and methods

2.1. Petrology

We used all the available whole rock composition and microchemical data on glasses, melt inclusions (MIs) and minerals for the MAV lavas and tephra. New mineral composition data collected by EPMA at the INGV of Roma from tephra are also presented. The whole dataset is reported in Tables S1, S2, S3, S4 and Figs. S1, S2, S3 and S4 in supplementary materials along with the data source. From the dataset, we select analyses with L.O.I. (loss of ignition) < 4 wt% and a total sum of major elements >96 wt% (Fig. S1).

Clinopyroxene (cpx) phenocrysts compositions from Tamburrino et al. (2015), Trua et al. (2002, 2014), Trua and Marani (2021) and this study (Fig. S2), were first tested for *equilibrium* (see Section 3.2), and then employed to calculate the temperature (*T*) and pressure (*P*) of crystallization using equations 33 and 30 of Putirka (2008). When available, we used the composition of the cpx_{core} (Table S4) coupled with the corresponding bulk chemistry of the coexisting liquid (Table S1). Only for the Tephra03 and Tephra04 (M3 and M4 in Tamburrino et al., 2015) we used crystal-glass couples (Table S2). The standard errors of estimate (SEE) are 170 MPa for pressure and 33 °C for temperature (Putirka, 2008). The calculated *P* values were adopted to

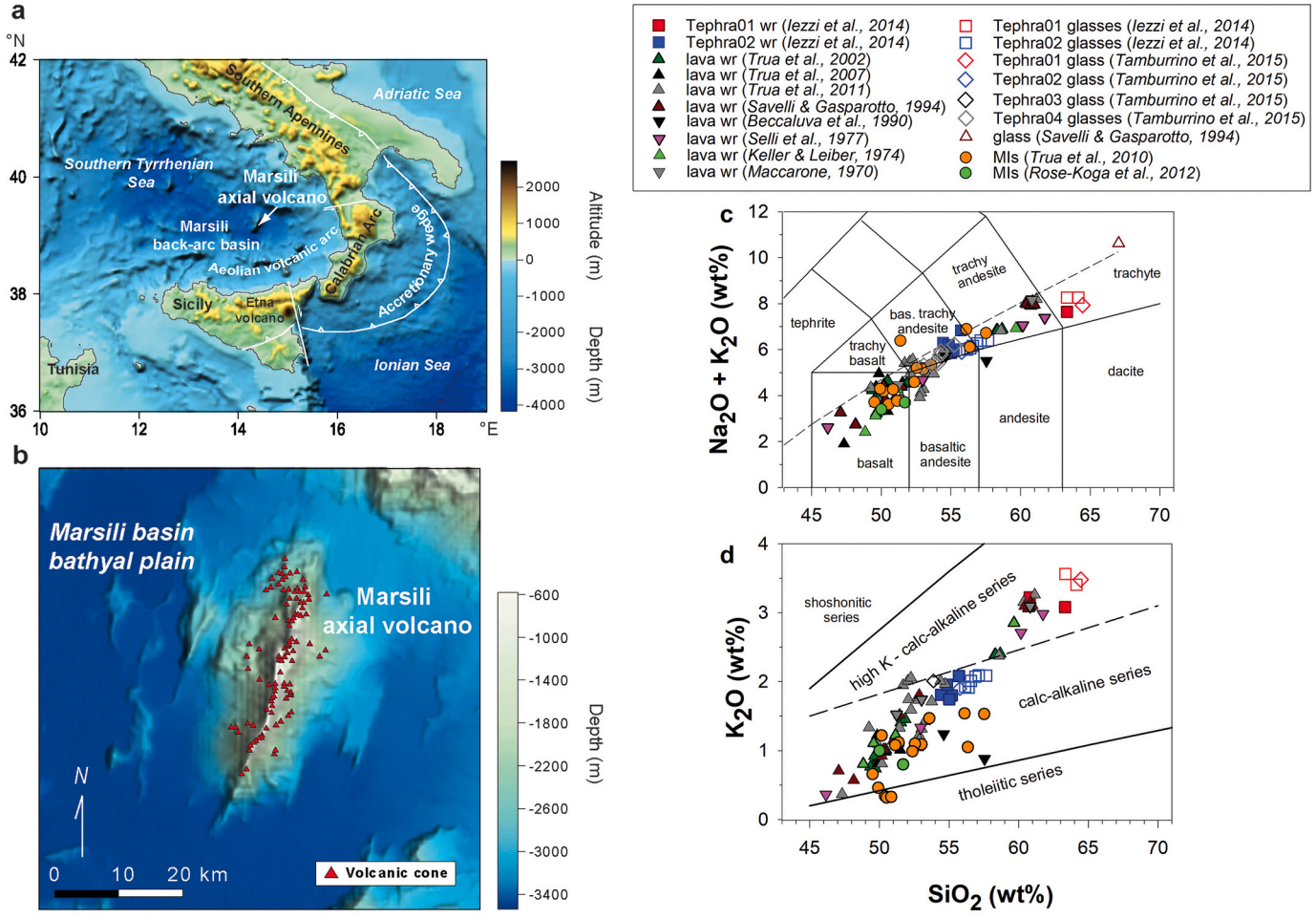

Fig. 1. a Location and geodynamic context of the MAV (bathymetry from EMODnet Bathymetry Consortium, 2020), and b 50 m resolution digital elevation model of the seamount (redrawn from Cocchi et al. (2009); distribution of volcanic cones (red filled triangle) is from Ventura et al. (2013). c TAS and d K_2O vs SiO_2 diagram of Marsili lavas and tephra (wr = whole rocks), glasses and melt inclusions (MIs). Samples are from literature (Beccaluva et al., 1990; Iezzi et al., 2014; Keller and Leiber, 1974; Maccarone, 1970; Rose-Koga et al., 2012; Savelli and Gasparotto, 1994; Selli et al., 1977; Tamburrino et al., 2015; Trua et al., 2002, 2007, 2010, 2011). Dashed line in plot 2c is the limit between alkaline and sub-alkaline fields (Irvine and Baragar, 1971). (For interpretation of the references to colour in this figure legend, the reader is referred to the web version of this article.)

estimate the storage depth of the magma(s) assuming an average density of the oceanic crust of 2700 kg/m^3 (as reported in Section 2.2). Anorthite (An) and Albite (Ab) components of plagioclase (plg) phenocrysts (from Tamburrino et al., 2015; Trua et al., 2002, 2014, 2017; and this study, Table S4 and Fig. S3) and the estimated *P* and *T* data are used as input parameters to calculate the H_2O amount following the hygrometer of Lange et al. (2009), for which the SEE is ±0.32 wt% H_2O. The model of France et al. (2010), which relates the partitioning of Fe^{3+} and Fe^{2+} among plg, cpx and the silicate melt, was used to constrain fO_2 (oxygen fugacity) in cpx- and plg-bearing rocks. For magnetite-bearing rocks, the partitioning of Fe and Ti between magnetite and the silicate melt (FeTiMM) was used to retrieve fO_2 (Arató and Audétat, 2017). The calculated *T*-*P*-H_2O-fO_2 values (Fig. 2, Table S5) are further validated by independent thermodynamic modelling with the MELTS code (Ghiorso and Sack, 1995; Smith and Asimow, 2005) at different *P*, fO_2 and H_2O content following Lanzafame et al. (2013) (Figs. S5, S6, S7, S8, S9 and Table S6).

2.2. Potential field data and modelling

A high-resolution gravity and magnetic ship-borne investigation of MAV was carried out in the Prometeous06 cruise (Cocchi et al., 2009). The total intensity magnetic field was recorded at 1 Hz (1 data per second) using a Geometrics G881 Cesium pumped magnetometer towed about 200 m astern the ship. Gravity data have been collected using a MicroG Air/Sea system II installed on-board the vessel. 1 Hz raw gravity readings were georeferenced using the DGPS system of the vessel. The raw gravity data were thus corrected for Eotvos effect and drift error. The two surveys were conducted in partly concomitance along a set of ESE–WNW parallel lines for a total length of 1400 km, with a line

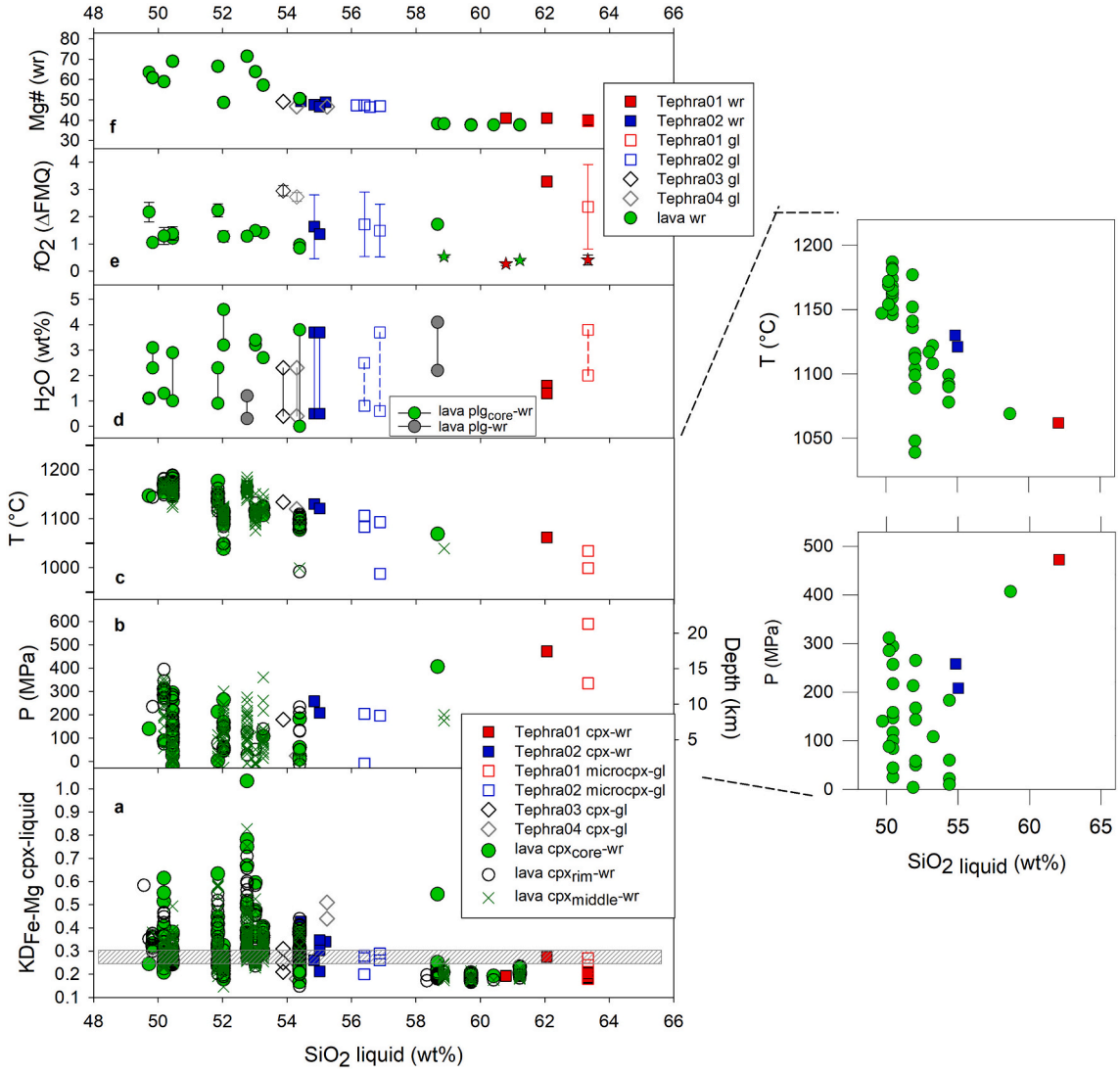

Fig. 2. a $KD^{cpx\text{-}liq}_{Fe\text{-}Mg}$ values calculated for all available cpx-melt couples; b pressure and c temperature computations (see text) for MAV rocks. For Tephra01: values are calculated using cpx and whole rock (wr) compositions respectively from Tamburrino et al. (2015) and Iezzi et al. (2014). Depths (below sea floor) are estimated assuming a density constraint of 2.7 × 10^3 kg/m^3 (see Section 2). d H_2O (wt%) abundance (estimated through the hygrometer of Lange et al. (2009) and e fO_2 has been estimated using *T* and *P* values calculated with Putirka (2008) only for *in equilibrium* cpx-melt couples ($KD^{cpx\text{-}liq}_{Fe\text{-}Mg}$ = 0.27 ± 0.03). For some lava rocks, H_2O has been calculated using, when available, An and Ab mol% of plg cores (green symbol). fO_2 reported in this plot is calculated through the models of Arató and Audétat (2017) (star symbols) and France et al. (2010), where values are indicated as variation (Δ) from the fO_2 of FMQ (Fayalite-Magnetite-Quartz) buffer. For the same tephra, the used *T*-*P* values are from microlites of cpx in *equilibrium* with glass (empty square symbols). SiO_2 and f Mg# of Marsili magmas are reported in these plots. On the right, simplified plots showing only values of *T* and *P* derived from *equilibrium* between whole rock and phenocryst or cpx (core), considered as the most significant couples. Acronyms: wr = whole rock, gl = glass, micro = microlites in matrix glasses. (For interpretation of the references to colour in this figure legend, the reader is referred to the web version of this article.)

spacing that ranges from 1200 m to 7000 m passing from the MAV summit ridge to the deeper and flat seafloor (Fig. S10). Further details about the data acquisition and processing methods can be found in Caratori-Tontini et al. (2010) and Cocchi et al. (2009). The joint interpretation of potential field data suggests the presence of a pervasive hydrothermal alteration affecting the MAV summit portion (Caratori-Tontini et al., 2010), a feature confirmed by the occurrence of low-temperature, sulphur-rich chimney fields (Ligi et al., 2014).

2.2.1. Gravity data reduction and estimation of Mantle Bouguer anomaly

The shipborne gravity measurements have been reduced by removing the gravimetric contribution produced by the density contrasts among water, crustal rocks and upper mantle (Fig. S10). Free air anomaly (FAA) field (Fig. 3b) has been derived by subtracting the latitude gravity contribution from the ship-borne measurements using WGS84 parameters. The contribution of each crustal layer in terms of gravity attraction was performed by applying an FFT technique based on Parker (1972), which involves a Taylor series expansion of powers of the Fourier transform. The Parker's algorithm requires a 2D discretization of two distinct surfaces and assumes a constant value of the contrast density between the two layers.

Complete Bouguer anomaly (CBA) was calculated by removing from the FAA data the gravity attraction derived by the density contrast between rocks at the seafloor (2700 kg/m^3) and the water layer (1030 kg/m^3) (Fig. S11a). In the estimation of the attraction from the upper mantle crustal interface, we assumed a crustal thickness of 9 km as defined by seismic data (Sartori et al., 2004). The gravity contribution of the mantle interface has been derived using a crustal-mantle density contrast of 500 kg/m^3 (average density of mantle equal to 3200 kg/m^3). Mantle Bouguer anomaly (MBA) has been thus obtained by subtracting this latter contribution from the previous CBA data (Fig. S11b).

2.2.2. 2.5D magnetic and gravity forward model

Magnetic and gravity data (Fig. 3a, b) are newly interpreted performing joint 2.5D forward models. This modelling technique, which is detailed in Cocchi et al. (2017), provides a detailed reconstruction of the crustal structure by means of a best fitting between the observed and computed profiles obtained varying the geometry, magnetic susceptibility and density of the causative bodies (Fig. 4). The model accounts for the variation of dimensions of the different rock bodies both along and symmetrically across the profile (2.5 dimension). Although this type of model may not have a unique solution, in this specific case density and depth of the different magma-rich bodies with variable SiO_2 content are reconstructed in agreement with the results from the petrological analysis, as previously reported (Fig. 2, Table S5).

2.2.3. 3D inverse gravity modelling

We derived a 3D reconstruction of the crustal structure of MAV by inverting the gravity anomalies. This interpretative approach is aimed at obtaining a 3D distribution of the density of the rocks forming the seamount able to reproduce the observed gravity anomalies. The inversion was performed using an algorithm proposed by Caratori Tontini et al. (2006) and details about the mathematical formalism are reported in their study. The modelling approach we follow to obtain the subsurface 3D density distribution of the sources consists in subdividing the crustal layer in a set of prismatic cells characterized by a constant density value and in performing a linear inversion of the gravity anomalies. More in general, the inversion of gravity (and magnetic) data suffers a non-uniqueness of the solutions, especially in case of an unconstrained approach. This indicates that the same distribution of the observed anomaly can be modelled using different distributions of the causative sources. In order to overcome this situation, we used a robust algorithm, which adopts a priori information in terms of regularization of the matrix of solution (Tikhonov and Arsenin, 1977). The adopted inversion approach allows to estimate in a mathematical way the depth

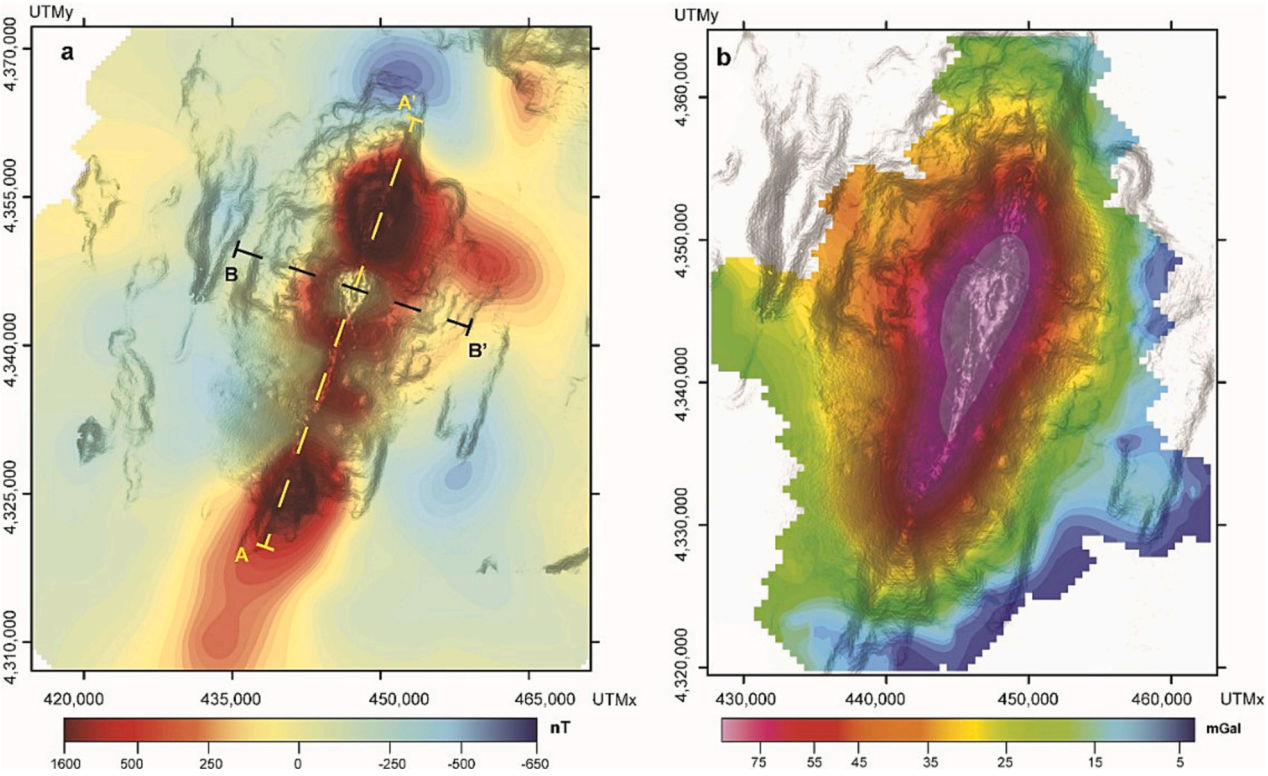

Fig. 3. a Shipborne magnetic anomaly and Free air gravity b data of MAV acquired during the Prometheus 06 cruise (R/V Minerva1). A-A' (yellow dashed line) and B-B′ (red dashed line) tracks identify the location of the magnetic and gravity profiles used in the forward models (Figs. 4 and S13). (For interpretation of the references to colour in this figure legend, the reader is referred to the web version of this article.)

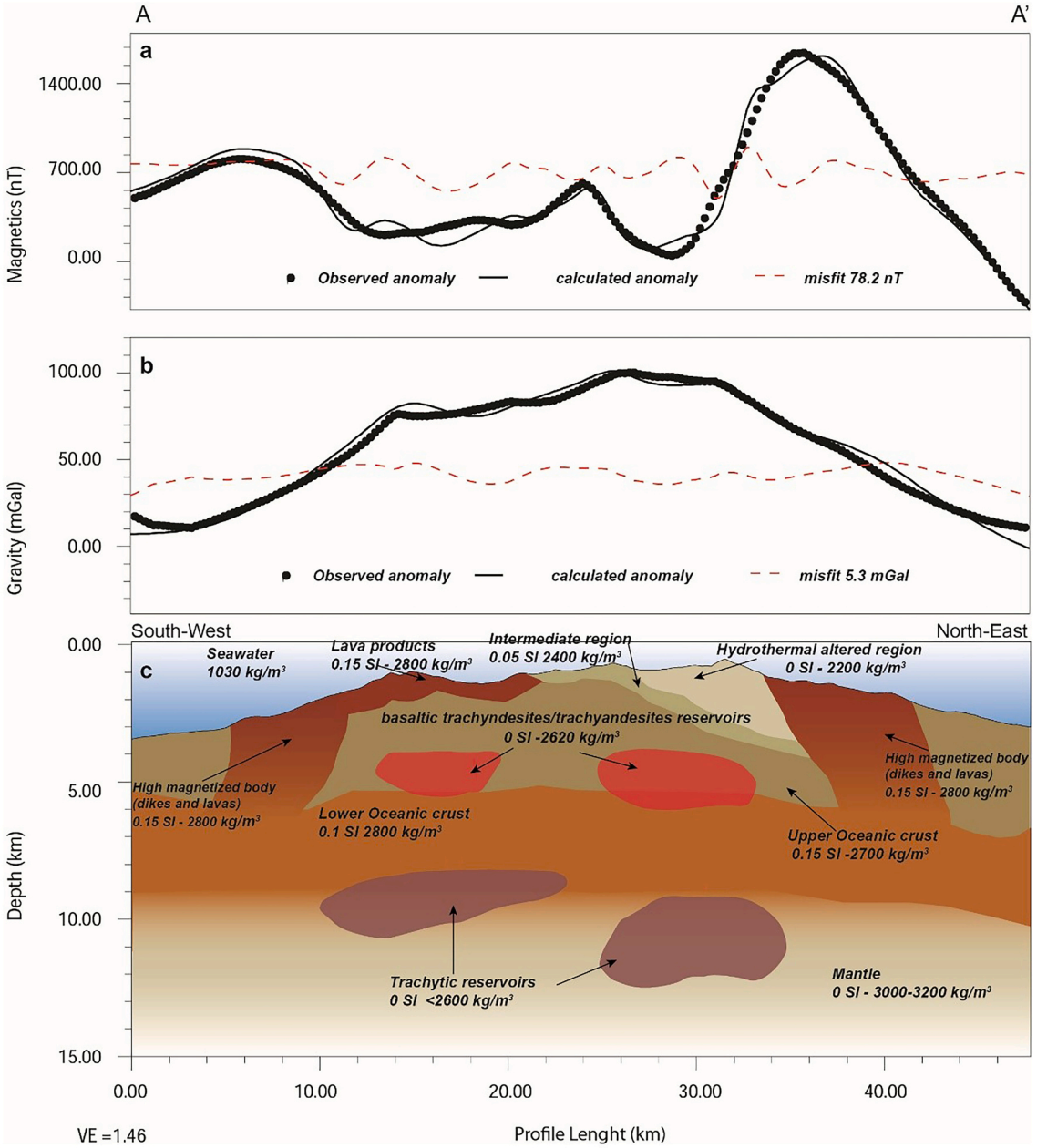

Fig. 4. Results of the 2.5D magnetic and gravity forward model of the Marsili Seamount. Magnetic and gravity anomaly data were sampled at 225 m along a NW-SE oriented profile (see track A-A' in Fig. 3a) along the major axis of the edifice. The best fit between observed and computed magnetic and gravity profiles are reported in panels a and b, respectively; c distribution of the causative bodies derived from a and b.

to the bottom distribution of the sources (DTB, see Caratori Tontini et al., 2006). This is achieved by analysing the distribution of the norm of solution vs residuals with a chi-square test. In the case of MAV, the DTB estimation provided a value of 10 ± 0.5 km; this value was used as a priori information for the subsequent inversion. We performed different inverse models with a rather similar geometry by varying different parameters such as the number of cells, the extension of the mesh, and the depth to the bottom interface. The optimal solution (minimum RMS misfit) was obtained using a prismatic mesh formed by 100x100x100 cells (equal to a cell-width of 360 m, 454 m and 95 m, in X, Y, and Z directions, respectively) with a vertical extension between the bathymetric surface and the DTB value.

The result of the gravity inversion is a 3D distribution of the density for the inner portion of the MAV region. We proposed a graphical representation using a set of isosurfaces (Fig. 5). These are 3D surfaces passing through points of equal density value. The graphical model was performed by using the Oasis Montaj software (Sequent inc.). The overall density distribution has been differentiated into four main layers: low (< 2500 kg/m^3), low to intermediate (2600–2650 kg/m^3), intermediate (2650–2750 kg/m^3) and high (> 2850 kg/m^3). This subdivision was logically defined to enhance both shallow and deeper sources. In particular, the low density layer highlights a set of sub circular structures aligned along the summit crest possibly reflecting local hydrothermal sources, as already provided by Caratori-Tontini et al. (2010). Additional density layers could be added (i.e. 2750–2850 kg/m^3), but these complicate the visualisation without improving the picturing of the inner structure of the volcano.

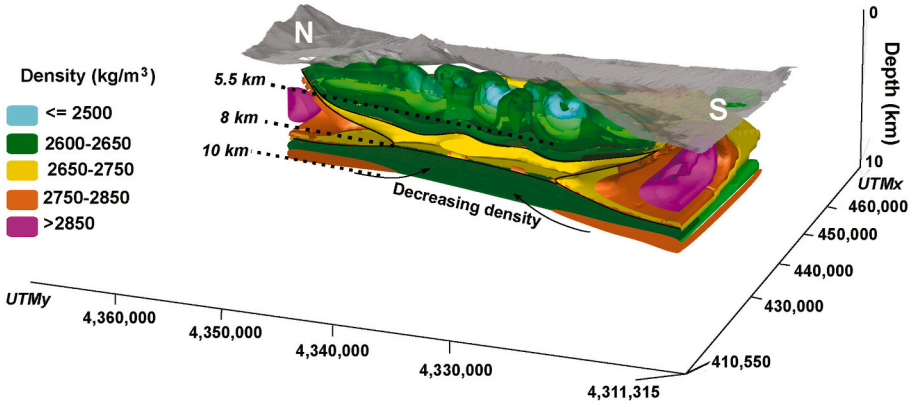

Fig. 5. Result of the 3D inversion of gravity data of MAV. The recovery density model has been cut by using a slice oriented in N-S (perspective view from SW) direction running along the main crest of the seamount.

3. Results

3.1. Petrologic features

The MAV rocks consist of lavas and tephra. The tephra are from wells located in the central, axial sector of the volcano and were erupted between 2.1 and 7.2 ka B.P. (Iezzi et al., 2014; Tamburrino et al., 2015). All the other products consist of lavas dredged on the flanks of the volcano. Because of the MAV steep slopes are affected by seafloor slides, the location of the lava samples may not mirror that of the corresponding lava flow. Therefore, the location of the lava flows is poorly constrained although these lavas are reasonably older than the tephra being the lava samples collected at greater depths (Trua et al., 2002).

The MAV rocks range in composition from basalts to trachytes with prevailing calc-alkaline and high-K calc-alkaline affinities; only a few MIs show a tholeiitic signature (Fig. 1c, d). The rocks depict a continuous and uninterrupted evolution trend (Fig. 1c) consistent with the dominant fractionation of early olivine, pyroxene, plagioclase, and later alkali-feldspar (Iezzi et al., 2014; Trua et al., 2002).

The chemical composition and the derived crystal-chemical formulas of the MAV minerals are reported in Table S4. Plagioclase is the most abundant phase followed by clinopyroxene and olivine. Plagioclase (Fig. S3) varies between andesine (An_{33}-Ab_{61}) and anorthite (An_{95}-Ab_{5}). Clinopyroxene occurs as phenocrysts and microlites and, regardless of the crystal size and bulk chemical composition of the tephra and lavas, its composition is augitic or close to the diopside-augite boundary (Fig. S2). Orthopyroxene ($En_{66–75}$) occurs in the intermediate and SiO_2-rich MAV rocks with restricted compositional variations (Fig. S2). Olivine phenocrysts are subordinated and range from Fo_{91} to Fo_{66} and few compositional differences exist between lavas and scorias. The amount of Fo molecule roughly decreases with the degree of evolution of the rocks (Fig. S4). Spinel is ubiquitous in lavas and it is found only in Tephra01 (Table S4). Spinel is Ti- and Mg-rich with a Usp component between 31 and 44 mol%, whereas Cr-spinels (up to 46 wt% of Cr_2O_3) are hosted in some basaltic lavas (Table S4). Few Ti-Mg-rich hastingsite and Fe-barroisite amphiboles occur only in the recent tephra, whereas apatite characterizes the evolved tephra and some andesitic lavas. Biotite occurs in the MRS4 basalt (Table S4).

3.2. T and P estimates

We determine *T* and *P* of crystallization from the analyses of clinopyroxenes with *equilibrium* $KD^{cpx\text{-}liq}_{Fe\text{-}Mg}$ values of 0.27 ± 0.03 (Fig. 2a, b, c and Table S5). The maximum *T* of crystallization of the MAV rocks linearly decreases from about 1200 °C to 1000 °C as a function of SiO_2. Nonetheless, the *T* recorded by clinopyroxene in SiO_2-poor rocks is variable being also lower than 1100 °C while the larger crystals document higher *T* than that of the tiny ones (Fig. 2c). The maximum estimated *P* values inferred by clinopyroxenes at *equilibrium* conditions follow a rough general increase from basalts to trachytes (Fig. 2b). In the more evolved MAV rocks, the larger clinopyroxenes and their cores (blue squares, $SiO_2 > 54.5$ wt% in Fig. 2) display a decrease of the *T* of crystallization coupled with an increase of *P* with the SiO_2 content (Fig. 2b, c inset). In lavas, the calculated *equilibrium* (cpx_{core}) *T* spans from 1039 °C (basaltic andesitic and andesitic lavas) to 1189 °C (basaltic lavas) (Fig. 2c and Table S5). The core of clinopyroxenes in the basaltic lavas virtually crystallized between 1136 °C and 1187 °C. The basaltic trachyandesite lavas show *T* between 1039 °C and 1122 °C (Fig. 2c). The estimated *P* values for the basalts and basaltic trachyandesitic lavas range between 4 and 311 MPa and between 10 and 265 MPa, respectively. These data suggest that the reservoirs of the basalts and basaltic trachyandesites are located at depth variable from the top of MAV down to 12 km b.s.f. (Fig. 2b and Table S5). In the trachyandesitic lavas, only few *equilibrium* $KD^{cpx\text{-}liq}_{Fe\text{-}Mg}$ are detected (for MRS9), with *T* and *P* in the ranges 1039–1069 °C and 175–407 MPa. These pressures correspond to a depth between 6.6 and 15.4 km b.s.f. (Fig. 2b, c and Table S5). Trua and Marani (2021) report *T* and *P* estimates only for the trachyandesite D14 with values in the ranges 1141–1145 °C and 80–100 MPa (~ 3 km depth). The clinopyroxene phenocrysts in the trachyandesitic and trachytic tephra crystallize at 1120–1130 °C and *P* of 208–258 MPa and 1062 °C and 472 MPa, respectively. These *P* values correspond to depths of 8–10 km b.s.f. and 17.8 km b.s.f. (Fig. 2b, c and Table S5). Based on our results, this latter value represents the deepest magma storage zone below MAV.

3.3. H_2O and fO_2 determinations

Only one study (Rose-Koga et al., 2012) reports direct measurements of H_2O contents of 1.6 and 2.1 wt% in melt inclusions (MIs) hosted in few MAV basaltic trachyandesites and basalts, although such determinations can underestimate the H_2O content due to H^+ diffusion (Lloyd et al., 2013). Therefore, we estimate H_2O in the MAV rocks using the hygrometer of Lange et al. (2009). All the MAV magmas record H_2O content unrelated to SiO_2 (and also with *T* and *P*) and invariably below 5 wt% with values generally in agreement with those of L.O.I. (Fig. 2d and Fig. S1).

The calculated fO_2 values indicate that the MAV rocks are slightly oxidized with fO_2 between 0.3 and 3.3 log units above the FMQ (Fayalite-Magnetite-Quartz) buffer (Fig. 2e) except for the lowest value (FMQ-0.9) for the olivine-hosted Ti-magnetite in MRS4 (rich in Cr-spinel). The more recent basaltic trachyandesitic and trachytic tephra are oxidized as the basaltic lavas (Fig. 2e). Our new range of fO_2 estimates extends the previous one (1.5–2.5 log units above the QFM buffer) calculated using olivine-spinel *equilibrium* (Ballhaus et al., 1991) in basaltic lavas (Trua

et al., 2014). The fO_2 of MAV rocks encompasses the redox fields of MORB (FMQ-1 < fO_2 < FMQ + 0.6), BAB (back-arc basalts, FMQ < fO_2 < FMQ + 3), OIB (FMQ < fO_2 < FMQ + 2) and IAB (FMQ + 1 < fO_2 < FMQ + 3) (e.g., Gaillard et al., 2015). In summary, only *T* and *P* of the MAV rocks are dependent on the degree of evolution of magmas (Fig. 2f).

3.4. Theoretical solidification path

Five representative MAV magmas with different degrees of evolution are used as starting composition for crystallization models with the MELTS code (Ghiorso and Sack, 1995; Smith and Asimow, 2005) at different *P*, fO_2 and H_2O content (Figs. S5, S6, S7, S8, S9 and Table S6). The conditions better reproducing the observed mineral assemblages (Figs. S2, S3, S4) and the *T*, *P*, fO_2 and H_2O values estimated from mineral equilibria (Fig. 2b, c, d, e) in the MAV basalts are attained with *P* = 100 MPa, fO_2 between FMQ + 1 and FMQ + 2, and H_2O = 0.5 wt% (Fig. S5). For the basaltic trachyandesites, the best conditions are at *P* and fO_2 of 100 MPa and FMQ + 1, respectively, and H_2O = 0.5 wt% (Fig. S6). The mineral assemblage of trachyandesites may be reproduced at 100 and 400 MPa, however, the clinopyroxene+plagioclase paragenesis is better captured at 400 MPa, FMQ + 1 and 1 wt% of H_2O (Fig. S7). For the mugearitic tephra, the modelling results are *P* of 300 MPa, FMQ + 0.5 and FMQ + 2 with 0.5 wt% of H_2O. These values are in very good agreement with the observed data (Fig. S8). For the trachytic tephra, the conditions are *P* = 400 MPa, FMQ + 1.5, and H_2O = 1 wt% (Fig. S9).

3.5. Magnetic and gravity anomalies

MAV shows a very peculiar magnetic pattern characterized by intense positive anomalies with maximum value >1500 nT and negative anomalies (Fig. 3). The general positive magnetic anomalies are related to the young age of MAV, which was emplaced in the last 1 Ma (Cocchi et al., 2009). The symmetrical negative magnetic anomalies placed on the seafloor basin and bordering the base of the eastern and western flanks of the seamount are related to the emplacement of spots of oceanic crust during reversal geomagnetic polarity (Late Matuyama, C1r, 1.77–0.78 Ma) as the result of back-arc spreading processes. The MAV summit shows a magnetic minimum interpreted as the result of widespread rock alteration due to the release of hydrothermal fluids (Caratori-Tontini et al., 2010; Ligi et al., 2014). At the northern and southern tips of MAV, two intense positive peaks occur. These anomalies show the maximum values (> 1500 nT) recorded in the Marsili basin area (Fig. 3). These two magnetic highs coincide with two sectors of MAV characterized by outcropping lava flows and dykes and interpreted as surface manifestation of fissural-like volcanism at the edges of the seamount (Ventura et al., 2013).

The Free Air anomaly (FAA) pattern of MAV mimics the bathymetry with the maximum anomaly value recorded at the summit area of the edifice (Fig. 3). MAV shows a general low FAA pattern in contrast to the overall gravity signature expected for an about 3 km high volcanic edifice measuring 70 km in length and 30 km in width. Caratori-Tontini et al. (2010) identify the presence of local gravity minima localized on the summit crest. They recognize a spatial relationship between magnetic and gravity lows due to hydrothermal alteration processes whose effect is a decrease in the magnetization and density of the volcanic rocks. The circulation of hydrothermal fluids seems to be superimposed (or associated) to a sill-like magmatic reservoir placed at very shallow depth (Ventura et al., 2013). Complete Bouguer Anomaly (CBA) computed using a reduction density of 2700 kg/m^3 (see Section 2) depicts a general low-density pattern of the whole MAV excluding its southern and northern edges. Here, positive CBA peaks coincide with the magnetic highs. The central portion of MAV is characterized by the presence of three major gravity minima distributed along the ridge axis, one coincident to the major magnetic low and the others located slightly southward (Fig. S11a).

The Mantle Bouguer Anomaly (MBA, Fig. S11b) is obtained by subtracting the predictable gravity signal due to the water/crust and crust/mantle boundaries from the free air anomaly data. This map shows two main local gravity lows localized at the centre of the volcano and in the southern sector. The bull-yes pattern observed in the MBA could reflect variations in crustal (i.e. hydrothermally altered regions) and upper mantle densities or both as convolution of the two gravity signals. To better constrain the possible depth position of the MBA minima, we performed a correlation between MBA and the low pass filtered CBA (LPBA, Fig. S11c) along a NNW-SSE striking profile running along the major axis of the volcano (track C-C′ in Fig. S11a). The low frequency contribution of CBA was computed by applying the 8-degree Butterworth filter using a cut-off central wavelength of 9 km. LPBA map highlights the gravity signal related to the deeper, higher density sources excluding in this way the local shallowest low-density sources located along the MAV ridge and associated with the hydrothermal alteration. This is confirmed by the complement of LPBA (Fig. S11d) computed by subtracting the LPBA signal from CBA, which shows a chaotic distribution of very short wavelength gravity anomalies without any indication of major gravity lows.

Along the MAV ridge, LBPA profile highlights the presence of two minima spatially correlated to the major deflections already depicted in the MBA profile (Fig. S12). This result implies that the deep crustal portion of the Marsili area is also characterized by two main low density sources probably located at the crust/mantle interface, i.e. at the Moho.

3.6. Geophysical modelling

The magnetic and gravity forward modelling approach is reported in Section 2. The results are summarized in Fig. 4 and refer to a 50 km long, NNW-SSE striking cross-section located along the crest of MAV (see track A-A' in Fig. 3a). The results of an additional *E*-W striking forward model are shown in Fig. S13. In the forward models, the density and SI values of the upper and lower oceanic crust and mantle are taken from Caratori-Tontini et al. (2010). The obtained forward models provide a detailed image of the inner structure of the MAV deep roots. The magnetic signature of the volcano shows two main positive peaks (about 1500 nT) localized in the northern and southern sectors of MAV. These two anomalies are related to 5–6 km wide highly magnetized bodies (0.15 SI) with a thickness of 3–4 km (Fig. 4). These bodies may be associated with the MAV dyke swarms. The two magnetic anomalies are separated by a magnetic low possibly associated with low-magnetized and low-density hydrothermally altered rocks.

The long wavelength gravity and magnetic contribution has been constrained by introducing the mantle/crust interface at 9 km based on the available seismic reflection data (Sartori et al., 2004). The low gravity and magnetic patterns observed along the crest of MAV have been modelled by adding two main magma reservoirs located at depth of about 5–6 km. The depth and density (2620 kg/m^3) of such magma reservoirs are constrained by the results of the petrology on the MAV basaltic trachyandesites and trachyandesites (Fig. 2). In particular, the models are constrained by fixing the depth of the potential magma reservoirs as a function of the magma composition determined from the above reported petrological data. The density of the magmas (Table S5) has been calculated as a function of the whole-rock composition, *T*, *P* and H_2O following Iacovino and Till (2019).

The lowest wavenumber gravity signature recorded at MAV also depicts the presence of a low-density crustal layer located at the Moho depth. This anomalous pattern can be ascribed to the presence of large magmatic reservoirs at the mantle/crust interface or below (depth > 13 km) possibly filled by low density (< 2600 kg/m^3) evolved magmas whose density is consistent with that of the MAV trachyte (Figs. 1, 2).

The obtained crustal geometry and the bodies identified in the model depicted in Fig. 3 have been used as the base for a sensitivity, back-validation analysis of our results. By fixing the depth and dimension

of the different generating bodies, we tested the effect of other possible different crustal configurations by (a) varying the density and magnetic susceptibility values and trying to exclude the deep and/or shallow magmatic reservoirs, (b) inverting the depth of the SiO_2-rich and SiO_2-poor magma reservoirs, and (c) excluding the presence of the hydrothermal alteration at the summit of MAV. The results of the sensitivity analysis from these alternative geologic models (Fig. S14e) show that their fit (Fig. S14a, c) to the observed data is significantly worse (Fig. S14b, d).

The 3D inversion of CBA data allows us to investigate the inner structure of the MAV region (Fig. 5). Inverse modelling has been achieved following Li and Oldenburg (1996) using a linear inversion between the observed anomaly data and the recovery of the 3D distribution of rock densities (see Methods). The recovery model highlights a very complex pattern of the densities of the sub-seafloor portion of MAV. The inverse model detects four major crustal layers (or domains) having slight differences in density (Fig. 5). The upper portion of the volcano, just below the MAV summit is featured by 3 semi-spherical sources having a length of some kilometre and relatively low-density values (2200–2500 kg/m^3). These bodies can be interpreted as shallow, probably altered rocks affected by the circulation of hot fluids. The recovery model highlights a region located at 5 km depth with density values of 2600–2650 kg/m^3 (dark green isosurface in Fig. 5). According to the results of the 2D model in Fig. 4, this region could be interpreted as basaltic trachyandesitic to trachyandesitic magma reservoirs possibly heating the overlying MAV hydrothermal system. Just below this region, the density increases to values of 2650–2750 kg/m^3 (yellow isosurface in Fig. 5). This layer could represent the inner, core complex of the volcanic edifice. Further below, we observe an unexpected decrease of the density (dark green isosurface) while the northern and southern edges of MAV are characterized by high density ($>$ 2850 kg/m^3) bodies. These two bodies could correspond to the two major basaltic dyke swarms already identified in the forward model of Fig. 4. The low-density body located at about 10 km depth may be interpreted as the reservoir(s) of evolved, trachytic magma.

4. Discussion

The MAV petrological data show that the younger spreading ridge of the Southern Tyrrhenian Sea back-arc basin erupted products ranging in composition from early basalt/trachybasalts up to later trachytic magmas originated by fractional crystallization processes (Trua et al., 2002, 2011) (Figs. 1c, d, S2, S3, S4). The evolution trend of the MAV magmas differs from that generally recognized in other spreading ridges, where evolved magmas are, with few exceptions, e.g. the Alarcon Rise rhyolites (Portner et al., 2022), generally lacking. The thermo-, baro-, hygro- and oxy-meters determinations on the MAV minerals (Fig. 2) are in agreement with the results from the independent thermodynamic simulations performed at variable T, P, H_2O and fO_2 (Figs. S5, S6, S7, S8, S9), and show that the SiO_2-poor and hotter magmas ascending from asthenosphere preferentially accumulate at variable crustal depth with pressure $\leq$ 300 MPa (Fig. 2b, c) on short time (days-few years) scales (Albert et al., 2022). The intermediate to high SiO_2 MAV magmas reside, on average, at deeper crustal levels down to the mantle-crust boundary at pressures between 200 MPa and 450 MPa (Fig. 2c). Their evolution degree requires residence times scales significantly longer than few years, although not quantifiable from the available data.

The results of the modelling of potential field data corroborate the vertical zonation of the MAV plumbing system inferred from the results of P and T estimates on the minerals (Fig. 4). In particular, models with denser large magmatic bodies, i.e. basalts, at crustal depths $>$10 km, are not feasible because of their greater misfit (Fig. S13). The 3D inversion of gravity data (Fig. 5) shows a general pattern of the central area of MAV where the density tends to decrease at greater depth (2600 kg/m^3 at depth $>$ 10 km), suggesting the presence of lower density magma placed at deep portions of the MAV plumbing system.

Our most reliable geophysical model is obtained by combining a set of SiO_2-poor magma reservoirs placed just below the base and within the MAV edifice with the trachyandesites preferentially stored at the boundary between the upper and lower oceanic crust and the more evolved magmas in sill-like reservoirs located at the Moho depth, i.e. at the crust/mantle interface. As a result, we propose that the major crustal interfaces below MAV play a major role in controlling the storage and differentiation zones of melts upraising from the mantle. This feature is not exclusive to MAV and has been observed in volcanoes at convergent (Koulakov et al., 2017) and intraplate (Li et al., 2021) geodynamic settings. At MAV, our estimate of the magma temperature at storage conditions for the trachytes is ~1060 °C (Fig. 2), a value corresponding to the temperature estimated below the Marsili back-arc basin at 10–15 km depth, i.e. at the Moho (Wang et al., 1989). The close correspondence between the inferred temperature and pressure of magma storage of the MAV trachytes and that of the Marsili basin back-arc rocks at the Moho indicates that the MAV evolved magmas are in thermal and barometric *equilibrium* with the surrounding rocks. In addition, the nearly constant values of the oxygen fugacity and water content of the MAV basalts, trachyandesites and trachytes (Fig. 2d, e) suggest that the plumbing system of the Marsili spreading ridge is characterized by homogenous redox and water content conditions. Our model implies that most of the not erupted basalts from which the trachytes evolve by crystal fractionation are stored below the Moho in the mantle.

The occurrence of evolved magmas in the deep levels of the MAV plumbing system may be explained by considering the model proposed by Annen et al. (2006) for the formation of deep magma storage of evolved magmas in the deep crust at subduction-related volcanoes. Following this model, the mantle-derived basalts emplace as a sequence of partly superimposed sills at the Moho and in the lower crust. This favours the formation and growth of a deep hot zone where the crystallization of basalts or the melting of the surrounding rocks may produce residual, SiO_2-rich magmas. This model explains not only the unusual vertical zonation of the MAV plumbing system, which is characterized by magmas originating from crystal fractionations but also the occurrence of granites and anorthosites hosted in the deep roots of ancient and active spreading centres and mainly associated with the melting of pre-existing rocks (Bennett et al., 2019; Koepke et al., 2007; Rollinson, 2014). The peculiar, vertical zonation of the MAV plumbing system is similar to that deduced from petrological data at some volcanoes of Aeolian Islands, which represent the volcanic arc of the Calabrian Arc subduction system (Fig. 1a, b). Some of these volcanoes on Lipari and Salina Islands are characterized by eruptions triggered by the arrival of deep-seated rhyolites in shallower, crystal-rich basaltic to andesitic magma chambers (Calanchi et al., 1993; De Rosa et al., 2003).

The occurrence of less dense, probably evolved magmas, in the deep roots of other submarine volcanoes of the Tyrrhenian Sea has been also suggested by geophysical data (Cella et al., 2006). Although the presence of deep, large, relatively cold and SiO_2-rich magma reservoirs placed below hotter and SiO_2-poor storage zones is a paradox from a thermal perspective, the 'reverse' zonation of the plumbing system of MAV and some of the surrounding Aeolian volcanoes can be explained by the presence of a continuous refilling of hot and hydrated basaltic melts from the asthenosphere (Corradino et al., 2022). We propose a conceptual model (Fig. 6) in which the basalts rising from the mantle may reach the surface along dykes or stop at the Moho depth or other intracrustal discontinuities as the upper/lower crust boundary depending on the magma supply and back-arc spreading rate (Cocchi et al., 2009; Ventura et al., 2013; Zitellini et al., 2019). In that last case, the fractional crystallization of basaltic magmas forms sill-like magma reservoirs with residual evolved melts. The higher viscosity of the MAV evolved magmas and the presence of physical discontinuities may favour the arrest, accumulation, and lateral expansion of magmas in reservoirs at depth (Giuliani et al., 2021; Lanzafame et al., 2017) (Fig. 3). Intermediate and SiO_2-rich magmas are then episodically remobilized and transported at shallower levels, where they can erupt as lava flows or

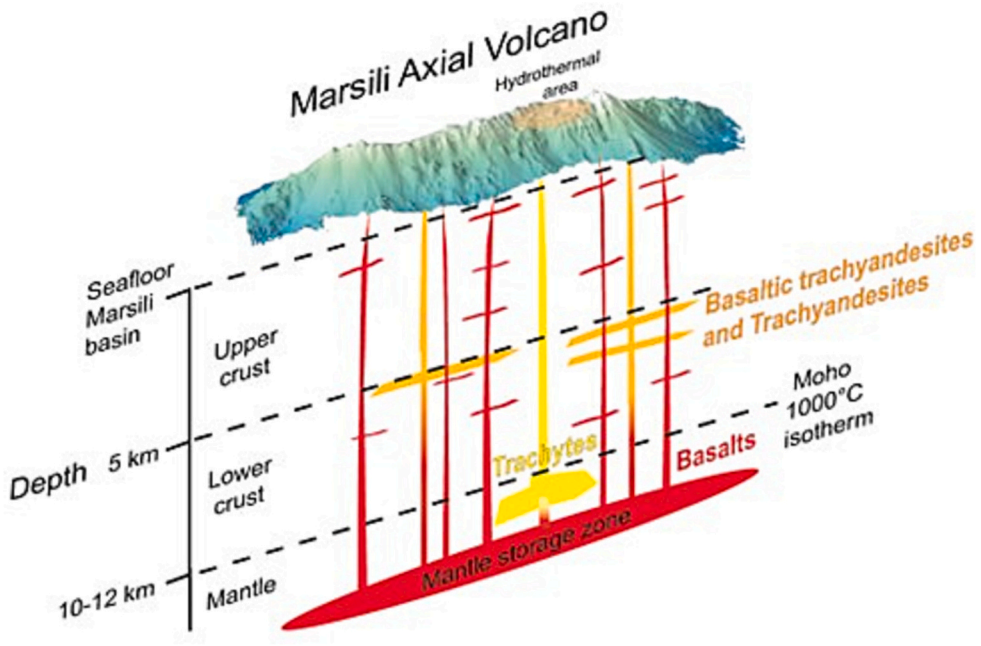

Fig. 6. Conceptual model of the MA*V* plumbing system deduced from integrated petrological and potential fields data.

explosively, as a function of the accumulation of gas bubbles (Iezzi et al., 2020). The high heat flow at shallower MAV levels is supplied by the continuous arrival (advection) of SiO_2-poor magmas along dykes while at depth there is a thermal *equilibrium* between the magmas hosted in the deeper reservoirs and the surrounding rocks, as previously reported.

The progressive decrease of the Marsili back-arc spreading rate from 2.8 to 3.1 cm/yr in the Matuyama (1.77 Ma) to 1.8 cm/yr during Jaramillo (1.07 Ma; Cocchi et al., 2009), and the more recent findings of the cessation of the back-arc spreading processes in the Marsili basin due to a compressional reorganization of the Southern Tyrrhenian Sea (Zitellini et al., 2019) could have favoured the formation of deep magma storage zones at MAV and the transition from an early, prevailing fissural basaltic volcanism to a later trachyandesitic to trachytic volcanism from localized vents (Iezzi et al., 2014, 2020; Ventura et al., 2013). The results of our combined petrological and geophysical study of MAV summarized in conceptual model of Fig. 6 show that the MAV plumbing system is not dissimilar to that already proposed for volcanoes in subduction and intraplate settings, where a vertical extension of the plumbing systems and the occurrence of deep-seated SiO_2-rich magma chambers has been already hypothesized (Annen et al., 2015; Cashman et al., 2017; Cruden and Weinberg, 2018; Magee et al., 2018; Sparks et al., 2012). The formation and growth of multi-level plumbing systems in spreading ridges of back-arc basins may be associated with a decrease in the spreading rates. Our results show that the integration of petrological and geophysical data validated by independent thermodynamic models and sensitivity analyses pave the way to further investigations on other seamounts or volcanoes worldwide and may reconcile the divergences observed between the results of geophysical and petrological models (Cashman et al., 2017).

5. Conclusion

We characterize the plumbing system of the Marsili back-arc spreading ridge by merging petrological and geophysical data. Results show the occurrence of different magma reservoirs with a sill-like shape located in the oceanic crust and within the volcanic edifice. Compositionally less evolved, high temperature magmas are stored at 10–12 km depth, whereas the more evolved melts show lower temperatures and greater storage depth (> 10 km up to 20 km).

We propose that the basaltic magma(s), originated at depth in the mantle, may have risen along fissures reaching the surface. Alternatively, this magma may have stopped at the Moho depth or at the upper/lower crust discontinuity, where it could evolve by fractional crystallization and form sill-like magma reservoirs. The larger sill-like reservoir with residual SiO_2-rich magmas located at the Moho may be remobilized and transferred to shallower depth, where it may erupts explosively or as lava flows. In back-arcs, the formation of deep, large magma chambers at the Moho is associated with a decrease in the spreading rate. The geometry of the plumbing system of oceanic spreading ridges at back-arc basins may be similar to that of the volcanoes located in convergent and intraplate settings.

Declaration of Competing Interest

The authors declare that they have no known competing financial interests or personal relationships that could have appeared to influence the work reported in this paper.

Data availability

All data supporting the findings of this study are available within the article and Supplementary Materials (see also the Methods section).

Acknowledgments

This study was funded by the PRIN (2009PZ47NA_003) project “Time Scales of Solidification in Magmas: Application to Volcanic Eruptions, Silicate Melts, Glasses, Glass-Ceramics” awarded to G. Iezzi. Most of this study was conducted during the post-doc (Assegno di Ricerca) of E. Gennaro. We thank the two referees for the perceptive and constructive comments, and our colleague Adam Smith for the revision of English.

Appendix A. Supplementary data

Supplementary data to this article can be found online at https://doi.org/10.1016/j.lithos.2023.107325.

References

Albert, H., Trua, T., Fonseca, J., Marani, M.P., Gamberi, F., Spiess, R., Marzoli, A., 2022. Time scales of open-system processes in a complex and heterogeneous mush-dominated plumbing system. Geology 50, 869–873. https://doi.org/10.1130/G49934.1.

Annen, C., Blundy, J.D., Sparks, R.S.J., 2006. The genesis of intermediate and silicic magmas in deep crustal hot zones. J. Petrol. 47, 505–539.

Annen, C., Blundy, J.D., Leuthold, J., Sparks, R.S.J., 2015. Construction and evolution of igneous bodies: towards an integrated perspective of crustal magmatism. Lithos 230, 206–221.

Arató, R., Audétat, A., 2017. FeTiMM – a new oxybarometer for mafic to felsic magmas. Geochem. Perspect. Lett. 5, 19–23. https://doi.org/10.7185/geochemlet.1740.

Ballhaus, C., Berry, R.F., Green, D.H., 1991. High-pressure experimental calibration of the olivine–orthopyroxene–spinel oxygen geobarometer: implications for the oxidation state of the upper mantle. Contrib. Mineral. Petrol. 107, 27–40.

Beccaluva, L., Bonatti, E., Dupuy, C., Ferrara, G., Innocenti, F., Lucchini, F., Macera, P., Petrini, R., Rossi, P.L., Serri, G., Seyler, M., Siena, F., 1990. Geochemistry and mineralogy of volcanic rocks from ODP sites 650, 651, 655, and 654 in the Tyrrhenian Sea. In: Proceedings of the Ocean Drilling Program, Scientific Results, p. 107.

Bennett, E., Frances, J., Millet, M.A., Cashman, K.V., Lissenberg, C.J., 2019. Deep roots for mid-ocean-ridge volcanoes revealed by plagioclase-hosted melt inclusions. Nature 572, 235–239.

Calanchi, N., De Rosa, R., Mazzuoli, R., Rossi, P., Santacroce, R., Ventura, G., 1993. Silicic magma entering a basaltic magma chamber: the case study of Salina (Aeolian Islands, Italy). Bull. Volcanol. 55, 504–522.

Caratori Tontini, F., Cocchi, L., Carmisciano, C., 2006. Depth-to-the-bottom optimization for magnetic data inversion: magnetic structure of the Latium volcanic region, Italy. J. Geophys. Res. 111, B11104.

Caratori-Tontini, F., Cocchi, L., Muccini, F., Carmisciano, C., Marani, M., Bonatti, E., Ligi, M., Boschi, E., 2010. Potential-field modeling of collapse-prone submarine volcanoes in the southern Tyrrhenian Sea (Italy). Geophys. Res. Lett. 37. L03305-1–L03305-5.

Cashman, K.V., Sparks, R.S.J., Blundy, J.D., 2017. Vertically extensive and unstable magmatic systems: a unified view of igneous processes. Science 355, eaag3055.

Cella, F., de Lorenzo, S., Fedi, M., Loddo, M., Mongelli, F., Rapolla, A., Zito, G., 2006. Temperature and density of the Tyrrhenian lithosphere and slab and new interpretation of gravity field in the Tyrrhenian Basin. Tectonophysics 412, 27–47.

Cocchi, L., Caratori-Tontini, F., Muccini, F., Marani, M., Bortoluzzi, G., Carmisciano, C., 2009. Chronology of the transition from a spreading ridge to an accretional seamount in the Marsili backarc basin (Tyrrhenian Sea). Terra Nova 21, 369–374. https://doi.org/10.1111/j.1365-3121.2009.00891.x.

Cocchi, L., Passaro, S., Tontini, F.C., Ventura, G., 2017. Volcanism in slab tear faults is larger than in island-arcs and back-arcs. Nat. Commun. 8, 1451. https://doi.org/10.1038/s41467-017-01626-w.

Corradino, M., Balazs, A., Faccenna, C., Pepe, F., 2022. Arc and forearc rifting in the Tyrrhenian subduction system. Sci. Rep. 12, 4728. https://doi.org/10.1038/s41598-022-08562-w.

Cruden, A.R., Weinberg, R.F., 2018. Mechanisms of magma transport and storage in the lower and middle crust—magma segregation, ascent and emplacement. In: Burkhardt, S. (Ed.), Volcanic and Igneous Plumbing Systems. Elsevier, Amsterdam.

D'Alessandro, A., D'Anna, G., Luzio, D., Mangano, G., 2009. The INGV's new OBS/H: analysis of the signals recorded at the Marsili submarine volcano. J. Volcanol. Geotherm. Res. 183, 17–29. https://doi.org/10.1016/j.jvolgeores.2009.02.008.

D'Alessandro, A., Mangano, G., D'Anna, G., 2012. Evidence of persistent seismo-volcanic activity at Marsili seamount. Ann. Geophys. 55, 2. https://doi.org/10.4401/ag-5515.

De Rosa, R., Donato, P., Gioncada, A., Masetti, M., Santacroce, R., 2003. The Monte Guardia eruption (Lipari, Aeolian Islands): an example of a reversely zoned magma mixing sequence. Bull. Volcanol. 65, 530–543. https://doi.org/10.1007/s00445-003-0281-2.

France, L., Ildefonse, B., Koepke, J., Bech, F., 2010. A new method to estimate the oxidation state of basaltic series from microprobe analyses. J. Volcanol. Geotherm. Res. 189, 340–346. https://doi.org/10.1016/j.jvolgeores.2009.11.023.

Gaillard, F., Scaillet, B., Pichavant, M., Iacono-Marziano, G., 2015. The redox geodynamics linking basalts and their mantle sources through space and time. Chem. Geol. 418, 217–233. https://doi.org/10.1016/j.chemgeo.2015.07.030.

Ghiorso, M.S., Sack, R.O., 1995. Chemical mass transfer in magmatic processes IV. A revised and internally consistent thermodynamic model for the interpolation and extrapolation of liquid-solid equilibria in magmatic systems at elevated temperatures and pressures. Contrib. Mineral. Petrol. 119, 197–212. https://doi.org/10.1007/BF00307281.

Giuliani, L., Iezzi, G., Mollo, S., 2021. Dynamics of volcanic systems: physical and chemical models applied to equilibrium versus disequilibrium solidification of magmas. In: Vetere, F. (Ed.), Dynamic Magma Evolution. John Wiley & Sons, Inc., pp. 101–132. Geoph. Monograph, 254, American Geophysical Union. Published 2021. ISBN: 9781119521136, chp. 5.

Hildreth, W., 2004. Volcanological perspectives on Long Valley, Mammoth Mountain, and Mono Craters: several contiguous but discrete systems. J. Volcanol. Geotherm. Res. 136, 169–198.

Iacovino, K., Till, C.B., 2019. DensityX: a program for calculating the densities of magmatic liquids up to 1,627 °C and 30 kbar. Volcanica 2 (1), 1–10. https://doi.org/10.30909/vol.02.01.0110.

Iezzi, G., Caso, C., Ventura, G., Vallefuoco, M., Cavallo, A., Behrens, H., Mollo, S., Paltrinieri, D., Signanini, P., Vetere, F., 2014. First documented deep submarine explosive eruptions at the Marsili Seamount (Tyrrhenian Sea, Italy): a case of historical volcanism in the Mediterranean Sea. Gondwana Res. 25, 764–774. https://doi.org/10.1016/j.gr.2013.11.001.

Iezzi, G., Lanzafame, G., Mancini, L., Behrens, H., Tamburrino, S., Vallefuoco, M., Passaro, S., Signanini, P., Ventura, G., 2020. Deep sea explosive eruptions may be not so different from subaerial eruptions. Sci. Rep. 10, 6709. https://doi.org/10.1038/s41598-020-63737-7.

Irvine, T.N., Baragar, W.R.A., 1971. A guide to the chemical classification of the common volcanic rocks. Can. J. Earth Sci. 8, 523–548. https://doi.org/10.1139/e71-055.

Keller, J., Leiber, J., 1974. Sedimente, Tephralagen und Basalte der südtyrrhenischen Tiefsee-Ebene im Bereich des Marsili-Seeberges. In: "Meteor" Forschungsergeb, 19, pp. 62–76.

Koepke, J., Berndt, J., Feig, S.T., Holtz, F., 2007. The formation of SiO_2-rich melts within the deep oceanic crust by hydrous partial melting of gabbros. Contrib. Mineral. Petrol. 153, 67–84.

Koulakov, I., Abkadyrov, I., Al Arifi, N., Deev, E., Droznina, S., Gordeev, E.I., Jakovlev, A., El Khrepy, S., Kulakov, R.I., Kugaenko, Y., Novgorodova, A., Senyukov, S., Shapiro, N., Stupina, T., West, M., 2017. Three different types of plumbing system beneath the neighboring active volcanoes of Tolbachik, Bezymianny, and Klyuchevskoy in Kamchatka. J. Geophys. Res. Solid Earth 122, 3852–3874. https://doi.org/10.1002/2017JB014082.

Lange, R.A., Frey, H.M., Hector, J., 2009. A thermodynamic model for the plagioclase-liquid hygrometer/thermometer. Am. Mineral. 94, 494–506. https://doi.org/10.2138/am.2009.3011.

Lanzafame, G., Mollo, S., Iezzi, G., Ferlito, C., Ventura, G., 2013. Unravelling the solidification path of a pahoehoe "cicirara" lava from Mount Etna volcano. Bull. Volcanol. 75-4, 1–16.

Lanzafame, G., Iezzi, G., Mancini, L., Lezzi, F., Mollo, S., Ferlito, C., 2017. Solidification and turbulence (non-laminar) during magma ascent: insights from 2D and 3D analyses of bubbles and minerals in an Etnean dyke. J. Petrol. 58, 1511–1534.

Li, Y., Oldenburg, D.W., 1996. 3-D inversion of magnetic data. Geophysics 61, 394–408. https://doi.org/10.1190/1.1443968.

Li, Y., Weng, A., Xu, W., Zou, Z., Tang, Y., Zhou, Z., Li, S., Zhang, Y., Ventura, G., 2021. The trans-lithospheric magma plumbing system of intraplate volcanoes as revealed by electrical resistivity imaging. Geology 49. https://doi.org/10.1130/G49032.1.

Ligi, M., Cocchi, L., Bortoluzzi, G., D'Oriano, F., Muccini, F., Caratori Tontini, F., de Ronde, C.E.J., Carmisciano, C., 2014. Mapping of seafloor hydrothermally altered rocks using geophysical methods: Marsili and Palinuro seamounts, southern Tyrrhenian Sea. Econ. Geol. 109, 2103–2117.

Lissenberg, C.J., MacLeod, C., 2016. A reactive porous flow control on mid-ocean ridge magmatic evolution. J. Petrol. 57 (11−12), 2195–2220. https://doi.org/10.1093/petrology/egw074.

Lloyd, A.S., Plank, T., Ruprecht, P., Hauri, E.H., Rose, W., 2013. Volatile loss from melt inclusions in pyroclasts of differing sizes. Contrib. Mineral. Petrol. 165, 129–153. https://doi.org/10.1007/s00410-012-0800-2.

Lupton, J., de Ronde, C., Sprovieri, M., Baker, E.T., Bruno, P.P., Italiano, F., Walker, S., Faure, K., Leybourne, M., Britten, K., Greene, R., 2011. Active hydrothermal discharge on the submarine Aeolian Arc. J. Geophys. Res. 116 https://doi.org/10.1029/2010JB007738.

Maccarone, E., 1970. Notizie petrografiche e petrochimiche sulle lave sottomarine del Seamount 4 (Tirreno Sud). Boll. Soc. Geol. Ital. 89, 159–180.

Magee, C., Stevenson, C.T.E., Ebmeier, S.K., Keir, D., Hammond, J.O.S., Gottsmann, J.H., Whaler, K.A., Schofield, N., Jackson, C.A.-L., Petronis, M.S., O'Driscoll, B., Morgan, J., Cruden, A., Vollgger, S.A., Dering, G., Micklethwaite, S., Jackson, M.D., 2018. Magma plumbing systems: a geophysical perspective. J. Petrol. 59 (6), 1217–1251. https://doi.org/10.1016/j.gloplacha.2015.07.005.

Marani, M.P., Trua, T., 2002. Thermal constriction and slab tearing at the origin of a superinflated spreading ridge: Marsili volcano (Tyrrhenian Sea). J. Geophys. Res. 107 (B9), 2188.

Parker, R.L., 1972. The rapid calculation of potential anomalies. J. R. Astron. Soc. 31, 447–455.

Portner, R., Dreyer, B.M., Clague, D.A., Daczko, N.R., Castillo, P.R., 2022. Oceanic zircon records extreme fractional crystallization of MORB to rhyolite on the Alarcon rise mid-ocean ridge. J. Petrol. 63 https://doi.org/10.1093/petrology/egac040.

Putirka, K.D., 2008. Thermometers and barometers for volcanic systems. Rev. Mineral. Geochem. 69, 61–120. https://doi.org/10.2138/rmg.2008.69.3.

Rollinson, H., 2014. Plagiogranites from the mantle section of the Oman Ophiolite: models for early crustal evolution. Geol. Soc. Spec. Publ. 392, 247–261.

Rose-Koga, E.F., Koga, K.T., Schiano, P., Le Voyer, M., Shimizu, N., Whitehouse, M.J., Clocchiatti, R., 2012. Mantle source heterogeneity for South Tyrrhenian magmas revealed by Pb isotopes and halogen contents of olivine-hosted melt inclusions. Chem. Geol. 334, 266–279. https://doi.org/10.1016/j.chemgeo.2012.10.033.

Rosenbaum, G., Lister, G.S., 2004. Neogene and Quaternary rollback evolution of the Tyrrhenian Sea, the Apennines, and the Sicilian Maghrebides. Tectonics 23, 1–17.

Sartori, R., Torelli, L., Zitellini, N., Carrara, G., Magaldi, M., Mussoni, P., 2004. Crustal features along a W–E Tyrrhenian transect from Sardinia to Campania margins (central Mediterranean). Tectonophysics 383, 171–192.

Savelli, C., Gasparotto, G., 1994. Calc-alkaline magmatism and rifting of the deep-water volcano of Marsili (Aeolian back-arc, Tyrrhenian Sea). Mar. Geol. 119, 137–157. https://doi.org/10.1016/0025-3227(94)90145-7.

Selli, R., Lucchini, F., Rossi, P.L., Savelli, C., Monte, M., 1977. Dati geologici, petrochimici e radiometrici sui vulcani centro-tirrenici. G. Geol. 42, 221–246.

Smith, P.M., Asimow, P.D., 2005. Adiabat_1ph: a new public front-end to the MELTS, pMELTS, and pHMELTS models. Geochem. Geophys. Geosyst. 6, Q02004. https://doi.org/10.1029/2004GC000816.

Sparks, R., Biggs, J., Neuberg, J., 2012. Monitoring volcanoes. Science 335, 1310–1311.

Tamburrino, S., Vallefuoco, M., Ventura, G., Insinga, D.D., Sprovieri, M., Tiepolo, M., Passaro, S., 2015. The proximal marine record of the Marsili Seamount in the last 7ka (Southern Tyrrhenian Sea, Italy): implications for the active processes in the Tyrrhenian Sea back-arc. Glob. Planet. Chang. 133, 2–16. https://doi.org/10.1016/j.gloplacha.2015.07.005.

Tikhonov, A.N., Arsenin, V.Y., 1977. Solutions of Ill-Posed Problems. Wiley, New York.

Trua, T., Marani, M.P., 2021. Clinopyroxene crystals in basic lavas of the Marsili volcano chronicle early magmatic stages in a back-arc transcrustal mush system. Geosciences 11, 159. https://doi.org/10.3390/geosciences11040159.

Trua, T., Serri, G., Marani, M., Renzulli, A., Gamberi, F., 2002. Volcanological and petrological evolution of Marsili Seamount (southern Tyrrhenian Sea). J. Volcanol. Geotherm. Res. 114, 441–464. https://doi.org/10.1016/S0377-0273(01)00300-6.

Trua, T., Serri, G., Marani, M., 2007. Geochemical features and geodynamic significance of the Southern Tyrrhenian backarc basin. In: Beccaluva, L., Bianchini, G., Wilson, M. (Eds.), Cenozoic Volcanism in the Mediterranean Area. GSA special publication, p. 418. Geological Society of America. https://doi.org/10.1130/2007.2418(11).

Trua, T., Clocchiatti, R., Schiano, P., Ottolini, L., Marani, M., 2010. The heterogeneous nature of the Southern Tyrrhenian mantle: evidence from olivine-hosted melt inclusions from back-arc magmas of the Marsili seamount. Lithos 118. https://doi.org/10.1016/j.lithos.2010.03.008.

Trua, T., Marani, M., Gamberi, F., 2011. Magmatic evidence for African mantle propagation into the southern Tyrrhenian backarc region. In: Volcanism and Evolution of the African Lithosphere, 478, p. 307. https://doi.org/10.1130/2011.2478 (16).

Trua, T., Marani, M., Barca, D., 2014. Lower crustal differentiation processes beneath a back-arc spreading ridge (Marsili seamount, Southern Tyrrhenian Sea). Lithos 190–191, 349–362. https://doi.org/10.1016/j.lithos.2013.12.014.

Trua, T., Marani, M., Gamberi, F., 2017. Magma plumbing system at a young back-arc spreading center: the Marsili Volcano, Southern Tyrrhenian Sea. Geochem. Geophys. Geosyst. 6 https://doi.org/10.1002/2017GC007151.

Ventura, G., Milano, G., Passaro, S., Sprovieri, M., 2013. The Marsili Ridge (Southern Tyrrhenian Sea, Italy): an island-arc volcanic complex emplaced on a 'relict' back-arc basin. Earth-Sci. Rev. 116, 8594.

Wang, C., Hwang, W., Shi, Y., 1989. Thermal evolution of a rift basin: the Tyrrhenian Sea. J. Geophys. Res. 94, 3991–4006.

Wanless, V.D., Shaw, A.M., 2012. Lower crustal crystallization and melt evolution at mid-ocean ridges. Nat. Geosci. 5 (9), 651–655.

Zitellini, N., Ranero, C.R., Loreto, M.F., Ligi, M., Pastore, M., D'Oriano, F., Sallares, V., Grevemeyer, I., Moeller, S., Prada, M., 2019. Recent inversion of the Tyrrhenian Basin. Geology 48. https://doi.org/10.1130/G46774.1.